Tunable Noncollinear Antiferromagnetic Resistive Memory through Oxide Superlattice Design

Jason D. Hoffman, Stephen M. Wu, Brian J. Kirby, and Anand Bhattacharya

Tunable Non-collinear Antiferromagnetic Resistive Memory through Oxide Superlattice Design

Jason D. Hoffman,[1, 2, *] Stephen Wu,[1, *] Brian J. Kirby,[3] and Anand Bhattacharya[1, 4, †]

[1]*Materials Science Division, Argonne National Laboratory, Argonne, Illinois 60439*
[2]*Department of Physics, Harvard University, Cambridge, Massachusetts 02138*
[3]*NIST Center for Neutron Research, National Institute of Standards and Technology, Gaithersburg, Maryland 20899, United States*
[4]*Nanoscience and Technology Division, Argonne National Laboratory, Argonne, Illinois 60439*

Antiferromagnets (AFMs) have recently gathered a large amount of attention as a potential replacement for ferromagnets (FMs) in spintronic devices due to their lack of stray magnetic fields, invisibility to external magnetic probes, and faster magnetization dynamics. Their development into a practical technology, however, has been hampered by the small number of materials where the antiferromagnetic state can be both controlled and read out. We show here, that by relaxing the strict criterion on pure antiferromagnetism, we can engineer a new class of magnetic materials that overcome these limitations. This is accomplished by stabilizing a non-collinear magnetic phase in $LaNiO_3/La_{2/3}Sr_{1/3}MnO_3$ superlattices. This state can be continuously tuned between AFM and FM coupling through varying either superlattice spacing, strain, applied magnetic field, or temperature. By using this new "knob" to tune magnetic ordering, we take a nanoscale materials-by-design approach to engineering ferromagnetic-like controllability into antiferromagnetic synthetic magnetic structures. This approach can be used to trade off between the favorable and unfavorable properties of FMs and AFMs when designing realistic resistive antiferromagnetic memories. We demonstrate a memory device in one such superlattice, where the magnetic state of the non-collinear antiferromagnet is reversibly switched between different orientations using a small magnetic field and read out in real time with anisotropic magnetoresistance measurements.

The field of spintronics uses the spin degree of freedom of the electron to realize electronic devices with novel functionalities not possible with just the charge degree of freedom. The central unifying element in almost all spintronic devices today is ferromagnetism (FM). In ferromagnetic materials, magnetization serves as a method to store information, as well as a mechanism to polarize electron spin. Pioneering work has recently explored the use of antiferromagnets (AFM) as a replacement for ferromagnetic materials in spintronics, since they produce no stray magnetic field and have faster magnetization dynamics (THz instead of GHz)[1–9]. These features may enable the development of smaller and faster spintronic devices and magnetic memories, overcoming current limits of scaling and speed for future spintronics applications.

The primary challenge to the realization of antiferromagnetic spintronics is the ability to both control and read out the AFM state reliably. So far, only a few materials have been discovered that demonstrate this effectively. One successful example is CuMnAs, where current-induced atomistic spin-orbit torques cause switching of the AFM state due to relativistic effects based on crystal symmetry[4]. Another is that of FeRh, where controlled magnetic field cooling from a high temperature FM state sets the AFM orientation at room temperature[3]. Since these effects rely on the unique properties of the individual materials, further development of AFM memories is limited by the inability to work with more general systems that can be tailored by materials design.

The synthesis of artificial magnetic multilayers offers an alternative approach, where new magnetic systems with tailored properties can be realized through materials growth[10]. Unfortunately, AFM systems created in this way suffer from the same problems of readability and controllability as traditional AFMs - to reset the magnetic state for memory operations requires either large magnetic fields or high temperatures to overcome the interlayer magnetic coupling or magnetic ordering temperatures. The approach that we follow here is to create synthetic structures that are intermediate between full antiferromagnetism and ferromagnetism in a *non-collinear* magnetic state (Fig. 1a). We retain the benefits of an AFM structure (small stray fields, fast dynamics), while gaining the controllability inherent to a FM. By continuously varying the non-collinearity in these systems, we create a "knob" that tunes the degree of AFM or FM-like properties. This approach can be used to trade-off between the favorable and unfavorable properties of each when developing real magnetic memories for applications.

Stabilizing non-collinearity in synthetic magnetic structures has been challenging due to the narrow window of precisely balanced interlayer exchange energies that is required[11–13], and has previously been observed in only narrow sub-angstrom regions of spacer thicknesses[14]. We have used polarized neutron reflectometry (PNR) to show that non-collinear magnetic structures can be stabilized across a wide-range of spacer layer thicknesses through the atomic-scale, layer-by-layer growth of $LaNiO_3/La_{2/3}Sr_{1/3}MnO_3$ (LNO/LSMO) superlattices[15]. Here, we demonstrate in one such superlattice the ability to tune continuously between FM and AFM magnetic structures (Fig. 1a) using applied
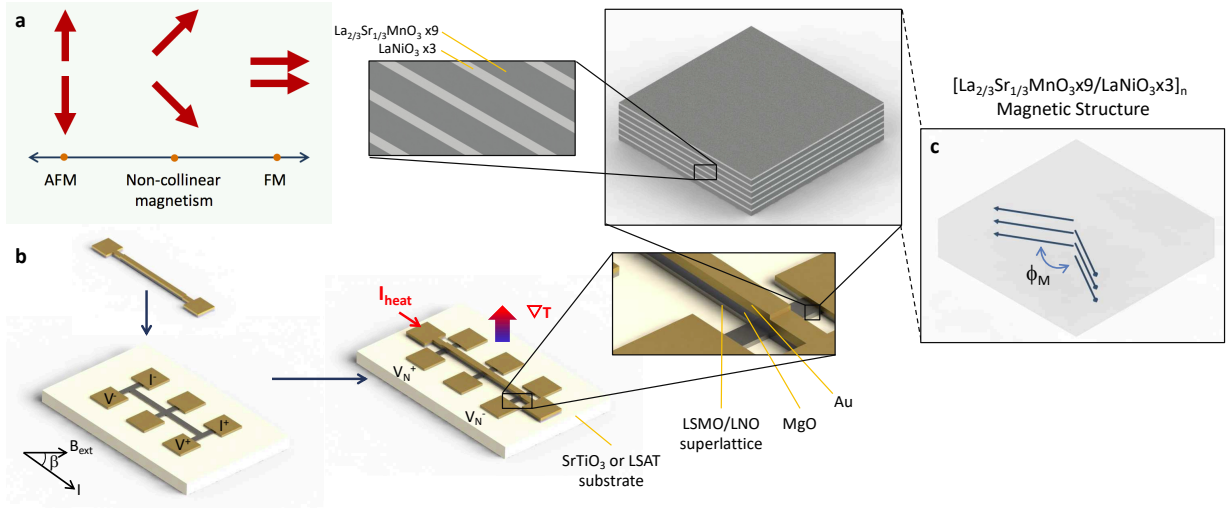
FIG. 1. **Schematic depiction of tunable non-collinear magnetic structures and device. (a)** An example of continuous tunability between a fully antiferromagnetic structure to a fully ferromagnetic structure, with non-collinear magnetism serving as the intermediate magnetic structure. **(b)** A patterned $[(LaNiO_3)\times3/(La_{2/3}Sr_{1/3}MnO_3)\times9]_n$ superlattice grown on $SrTiO_3$ (001), built into a Hall-bar device with on-chip heating for simultaneous anisotropic magnetoresistance and anomalous Nernst measurements. **(c)** The layer by layer magnetic structure of each LSMO layer within the superlattice, showing non-collinear interlayer magnetic coupling.

magnetic field, temperature, and substrate driven strain engineering. We also show the ability to fully map out the non-collinear magnetic state of micron-scale non-collinear memory devices using magnetotransport measurements. In this way, we have developed a nanoscale "materials by design" approach to create new, nearly AFM resistive memories that satisfy the conditions of controllability and readablity. This provides for an easy method of selecting the desired amount of AFM or FM-like properties, and is shown to be in full agreement with quantitative results we have obtained from polarized neutron reflectometry and magnetothermal measurements (Figs. 1b,c). By using only a small magnetic field, the magnetic state of the superlattice can be deterministically switched between eight stable states and read out using anisotropic magnetoresistance, while retaining the non-collinear magnetic structure (and therefore the advantageous AFM properties).

For this study, we have grown $\left[(LaNiO_3)_3 / (La_{2/3}Sr_{1/3}MnO_3)_9\right]_{14}$ superlattices by ozone assisted molecular beam epitaxy on (001)-oriented $SrTiO_3$ (STO) or $(LaAlO_3)_{0.3}$-$(Sr_2AlTaO_6)_{0.7}$ (LSAT) substrates. The base pressure in the chamber is $\lesssim 10^{-10}$ Torr, while the ozone partial pressure is maintained at 2×10^{-6} Torr during growth. A growth temperature of 600°C is used for both LNO and LSMO. Layer-by-layer growth was confirmed by monitoring the intensity oscillations of reflection high-energy electron diffraction (RHEED) peaks. High-resolution synchrotron diffraction measurements confirm the epitaxial growth of (001) LNO and LSMO layers and that the superlattice structures are coherently strained to the underlying substrate. The atomic abruptness of the interfaces is verified by

resonant x-ray reflectivity and scanning transmission electron microscope electron energy loss spectroscopy (STEM-EELS) measurements. The superlattice on STO was patterned into a Hall bar configuration with an electrically isolated on-chip heater for simultaneous magnetotransport and magnetothermal transport measurements using standard photolithography and ion-milling techniques (Fig. 1b)[16,17].

I. POLARIZED NEUTRON REFLECTOMETRY

The magnetic depth profile within the superlattices is first ascertained from polarized neutron reflectometry (PNR) measurements using the Polarized Beam Reflectometer at the NIST Center for Neutron Research. The superlattices were cooled from room temperature to 10 K or 125 K (for the sample on LSAT) or 110 K (for the sample on STO) in a magnetic field of 5.0 ± 0.5 mT, applied along the [100] direction. The magnetic field was then reduced to 1.2 ± 0.2 mT prior to the PNR measurements, which were carried out while monotonically increasing the field up to 700 mT. We measured both the non-spin-flip reflectivities, $R^{\uparrow\uparrow}$ and $R^{\downarrow\downarrow}$, and the spin-flip reflectivities, $R^{\uparrow\downarrow}$ and $R^{\downarrow\uparrow}$, which allows us to determine the depth-dependent magnitude and orientation of the magnetization within the superlattices.

We use the Nelder-Mead method within the REFL1D software package[18] to carry out quantitative fitting of the PNR data. In addition to the magnetic properties of the superlattice, we are able to determine the nuclear scattering length density, layer thickness, and interlayer roughness. These values are consistent with those measured at
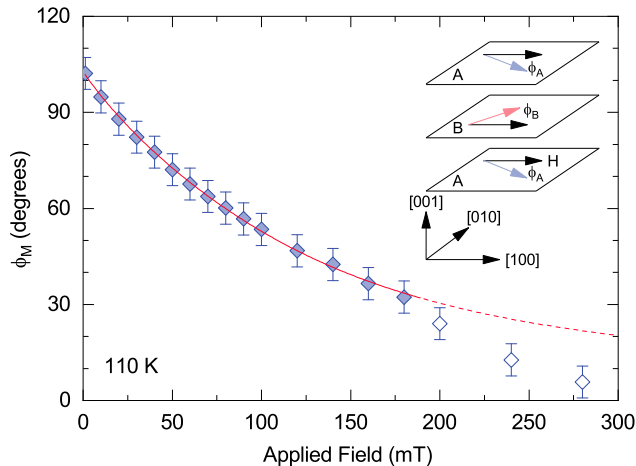
FIG. 2. **Polarized neutron reflectometry of the LNO/LSMO superlattice on SrTiO$_3$.** Magnetic field dependence of non-collinearity $\phi_M = |\phi_A - \phi_B|$ obtained from quantitative analysis of the spin-polarized neutron reflectometry spectra at 110 K with H along the [100] direction. The red line represents a fit based off of the free energy minimization model of the individual LSMO layers described in the text. The inset shows a schematic of the non-collinear magnetic configuration.

room-temperature using high-resolution x-ray diffraction and x-ray reflectivity. More than 30 magneto-structural models (e.g., a uniform magnetization profile within the LSMO layers versus a profile with reduced magnetization at the interface with LNO) are considered for each PNR data set, and the errors reported here are the standard deviation of the model-to-model variation in the fitted value of ϕ_M. Convergence was typically achieved within 5,000 iterations, but up to 250,000 iterations were required for models with many free parameters.

This data agrees with previous work[15] and has shown that the magnetic structure consists of individual LSMO magnetic planes stacked non-collinearly, as shown schematically in Fig. 1c and Fig. 2 (inset) . The angle between the magnetization of neighboring LSMO layers is $\phi_M = |\phi_A - \phi_B| = 104° \pm 3°$ at 110 K for the superlattice grown on STO and $\phi_M = 131° \pm 3°$ at 10 K and $\phi_M = 125° \pm 3°$ at 125 K for the superlattice on LSAT. Here, the degree of non-collinearity is likely

modified between the two superlattices due to substrate induced strain from the differences in lattice mismatch between the superlattice and STO/LSAT.

Figure 2 shows how the degree of non-collinearity of the magnetization varies as a magnetic field is applied along the [100] crystalline axis. We observe a monotonic decrease in ϕ_M with increasing magnetic field, as the magnetization of the LSMO sublattices align with the applied field. In previous work, we showed that this behavior cannot be explained using the "standard model" of bilinear and biquadratic magnetic coupling between the LSMO layers[15]. Rather, the best fit is obtained by assuming that a non-collinear magnetic structure within the LNO layers "biases" the angle between the LSMO layers at a value that depends on the LNO thickness. To model the evolution of ϕ_M, we numerically calculate the equilibrium positions of the sublattice magnetizations within the superlattice with respect to the in-plane field by minimizing the free energy per unit area. For a single interface,

$$E = -HMt \cos\left(\beta - \phi_i\right) + Kt \cos\left(4\phi_i\right) - J_{\text{int}} S_{\text{Mn}} S_{\text{Ni}} \cos\left(\phi_i - \phi_i^0\right), \tag{1}$$

where H is the applied field, M and t are the saturation magnetization and thickness of the LSMO layer, K is the first-order magnetocrystalline anisotropy constant of LSMO, which has easy axes along the $\langle 110 \rangle$ azimuths[19–21], J_{int} is the interface coupling constant, S_{Mn} and S_{Ni} are the interface magnetic moments for the LSMO and LNO layers, respectively, and $i = A, B$ identifies the LSMO sublattice. The angles β, ϕ_i, and ϕ_i^0 denote the direction of the applied magnetic field, the

orientation of the LSMO magnetization vectors, and the field-independent orientation of the interfacial LNO magnetic moments, respectively (see Fig. 2 (inset)). We ignore the detailed magnetic structure of the LNO layer.

We apply a least-squares minimization routine to the low-field regime (1.2 mT $\leq \mu_0 H \leq$ 180 mT) to determine the values of K, J, and ϕ_i^0 that best fit the measured field dependence of ϕ_M. The results are shown by the solid line in Fig. 2, which matches well with the measured

data and predicts an asymptotic approach to alignment. Above 200 mT, however, we find a more rapid decrease in ϕ_M than predicted by equation 1, which may arise from changes to the spin configuration within the LNO layers. From this analysis, we find that $J_{\text{int}} S_{\text{Mn}} S_{\text{Ni}} = 4.2 \times 10^{-5}$ J/m^2, $\left| \phi_B^0 - \phi_A^0 \right| = 138.5°$, and $K = 2.3 \times 10^3$ J/m^3, in agreement with values of K reported previously for perovskite manganite thin films[22–25].

II. MAGNETOTHERMAL MAPPING OF IN-PLANE MAGNETIZATION

With the magnetic structure of the LNO/LSMO superlattice known, it is now possible to design a device that allows the magnetic state of the devices to be read out in real time using only transport measurements. We take advantage of the anomalous Nernst effect (ANE) as a proxy measurement for in-plane magnetization. This is the magnetothermal transport equivalent of measuring out-of-plane magnetization using the anomalous Hall effect. To do this, we designed the device depicted in Fig. 1b to perform simultaneous magnetothermal and magnetoresistive transport measurements in an on-chip heating device geometry[17]. Hall bar structures (400 μm $\times$ 10 μm) were patterned using standard photolithography and liquid nitrogen cooled argon ion milling. For Nernst effect measurements, a 100 nm layer of electrically insulating MgO and a 20 nm layer of resistive Au were were deposited to create a heater. By applying 8.3 mW$_{rms}$ to the Au layer, an out-of-plane thermal gradient is created and a voltage develops across the heated superlattice layer that is proportional to the in-plane magnetization perpendicular to the axis of the device. This is due to the anomalous component of the Nernst effect generating, $\mathbf{E}_{ANE} \propto \nabla T \times \mathbf{M}$, where $\mathbf{E}_{ANE}$ is the electric field generated in the material due to the anomalous Nernst effect, ∇T is the thermal gradient across the material, and $\mathbf{M}$ is the magnetization of the material.

By performing the measurement on two separately fabricated devices on the same superlattice film with device axes oriented along both the $x \parallel [100]$ and $y \parallel [010]$ direction, we can fully map out the in-plane magnetization as the magnetic field is swept 360° in-plane (Fig. 3). At 100 mT, the non-collinearity is reduced from its low-field value (Fig. 2), such that the magnetization is primarily oriented along the applied field direction. Because the biaxial anisotropy is weak, the measured Nernst loops are nearly circular.

Small magnetic fields deterministically switch the magnetization between *eight* energetically favored orientations that are dictated by magnetocrystalline anisotropy (two distinct sets of four symmetry-equivalent states, see Fig. S1 [26]). This behavior is unique to our non-collinear magnetic superlattices and is reflected in the distinctive "daisy" pattern observed in Fig. 3a. To understand the switching behavior of the superlattice, we calculated the equilibrium orientation of the magnetization with respect

to a rotating in-plane magnetic field using the free energy minimization model (Eqn. 1) with the same values of K, J, and ϕ_0 used to fit the PNR data shown in Fig. 2. With this simple model, we find remarkable agreement between the measured and calculated magnetization maps, including the dip behavior for fields applied away from the primary crystallographic axes. Figures 3c,d show the calculated equilibrium configurations for fields of 5 mT and 100 mT applied along $\beta = 31.2°$ and $\beta = 0.0°$, respectively. For 5 mT, the calculations predict a dramatic enhancement of ϕ_M from 105° to 157° as the magnetic field is rotated away from the [100] axis, as shown by the blue arrows in Fig. 3c. Thus, by controlling the magnitude and orientation of the applied magnetic field, we are able to "park" our memory element in a state where advantageous AFM properties are maximized.

III. ANISOTROPIC MAGNETORESISTIVE READOUT OF NON-COLLINEAR MAGNETIC STATE

Anisotropic magnetoresistance (AMR) measurements provide a direct probe of the orientation of the magnetization of the conducting LSMO layers in our LNO/LSMO superlattices. Phenomenologically, the AMR of a ferromagnetic film with in-plane magnetization is

$$R^{xx} = R_\perp + \left(R_\parallel - R_\perp \right) \cos^2 \phi, \tag{2}$$

where ϕ is the angle between the magnetization and current, and $R_\parallel$ and $R_\perp$ denote the in-plane resistances for current oriented parallel ($\phi = 0°$) and perpendicular ($\phi = 90°$) to the magnetization, respectively[19,27,28].

Figure 4 shows the AMR $= \left[R\left(\beta \right) - R\left(\beta = 0° \right) \right] / R\left(\beta = 0° \right)$ signal measured at 110 K as the in-plane magnetic field is rotated relative to the current direction. At fields below around 20 mT, the curves have a distinct square shape due to the biaxial magnetocrystalline anisotropy[21,29,30]. Additionally, there is a hysteresis that appears at the two lowest fields representing a lag between the applied magnetic field and the response of the superlattice. At higher fields (Fig. 4f), where the magnetization of each LSMO layer is nearly aligned with the applied field, the AMR follows a typical $\cos^2 \beta$-dependence. The amplitude of the measured AMR signal (0.1 – 0.2%) is comparable to that found for existing single phase antiferromagnetic systems, such as Fe$_{1-x}$Rh$_{1+x}$[3], CuMnAs[4], and Sr$_2$IrO$_4$[5]. It may be possible to increase the size of the AMR effect in our superlattice devices by changing the composition of the manganite layer[31].

The most striking feature in the AMR measurements is the sign change between AMR measured at low (Figs. 4b-d) and high magnetic fields (Fig. 4f). This effect is due solely to the non-collinear layered magnetic structure in our system and can be qualitatively explained by considering the parallel contribution to the AMR from
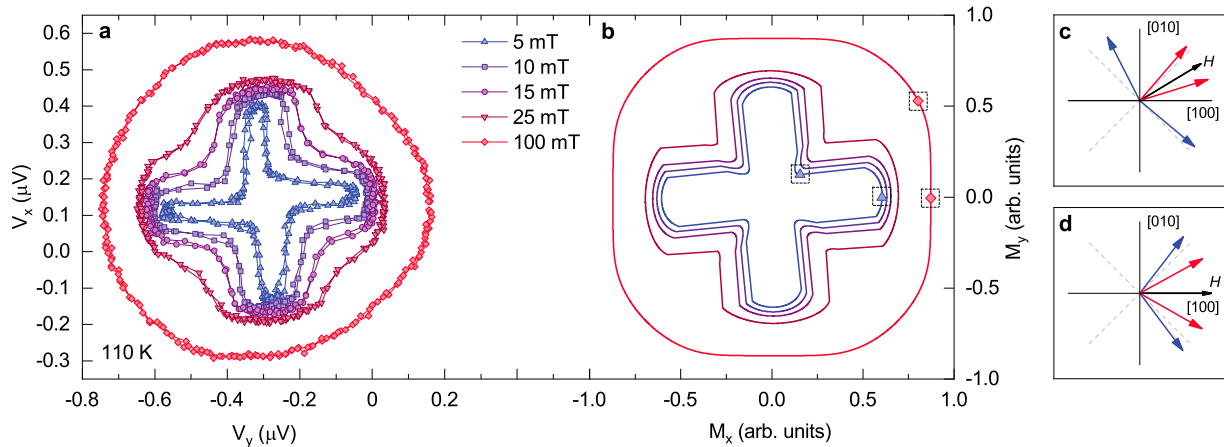
FIG. 3. **Anomalous Nernst effect measurements of in-plane magnetization for superlattice on SrTiO$_3$.** **(a)** Anomalous Nernst measurements on two devices oriented 90° to each other, measuring components of the in-plane magnetization along the $x \parallel$ [100] and $y \parallel$ [010] with respect to a 360° sweep of magnetic field at various field strengths. V$_x$ and V$_y$ are the voltages measured on Nernst devices that correspond to the effective magnetizations in the y and x directions, respectively, due to the relation $\mathbf{E}_{ANE} \propto \nabla T \times \mathbf{M}$. The measurements were performed at 110 K with 8.3 mW$_{rms}$ applied to the heater after magnetic field cooling from room temperature in 2.5 mT. The anomalous Nernst voltages measured in this device represent an in-plane magnetization map of the non-collinear magnetic state within the LNO/LSMO superlattice. **(b)** Simulation of the in-plane magnetization map based off the parameters obtained from PNR data and the free energy minimization routine. **(c)** and **(d)** Visualizations of the individual layer magnetization vectors at several points from (b) H = 5 mT (blue arrows) and H = 100 mT (red arrows) for fields applied at β = 31.2° (c) and β = 0.0° (d) from the [100] axis.

each LSMO layer (see Supplementary Information). In small magnetic fields, where $\phi_M > 90°$, the magnetization vectors of each individual layer have their largest components in a direction perpendicular to the applied magnetic field. Thus, the AMR signal is 90° out-of-phase with the direction of the magnetic field. In larger magnetic fields, $\phi_M < 90°$ and the magnetization of each layer is primarily oriented along the field (Fig. 4f) such that normal AMR behavior is recovered. This phase shift manifests itself as a sign change in our AMR measurements with increasing applied magnetic field. At intermediate fields (Fig. 4e) where ϕ_M is close to 90°, the AMR signals from neighboring layers nearly compensate each other and therefore the resistance modulations are strongly suppressed (see Supplementary Information).

To understand the observed AMR behavior we use the same values of K, J, and ϕ_0 found previously and field-independent values $R_\perp$ and $R_\parallel$ to calculate the longitudinal resistance AMR as a function of magnetic field direction. The predicted behavior matches exactly that shown in Fig. 4 and is plotted against the measured data as solid lines. Almost all the features in AMR are reproduced in this simple model using only parameters derived from the fits to the PNR data.

Figure 4g-k shows the AMR measured at a fixed magnetic field while the temperature is varied. We see that as temperature is increased, the degree of non-collinearity shrinks from an initial $\phi_M > 90°$ below 210 K, to $\phi_M < 90°$ at 230 K. This behavior is supported by temperature dependent PNR measurements, which show a monotonic decrease in coupling angle as the temperature

approaches the Curie temperature of around 265 K[15], and represents another way to continuously tune non-collinearity in these artificially designed magnetic materials.

IV. NON-COLLINEAR MAGNETIC RESISTIVE MEMORY OPERATION

Putting together the combined findings of this work, we now propose several mechanisms for the operation of a magnetic memory device with tunable non-collinearity. We have shown that at low temperatures, it is possible to design a nearly AFM structure where the magnetic state can be controlled with a small field B$_{rotate}$ while preserving the benefits of AFM memory (Fig. 5a). Using this approach, the magnetic state at 110 K can be repeatedly switched by alternately applying a field of 5 mT along the [100] and [010] axes, as shown Fig. 5c.

Since non-collinearity can also be tuned with temperature, an alternative mechanism for operation is first heating to a higher temperature where the degree of non-collinearity is lower, applying a smaller field to rotate the moment, then cooling back down to a stable nearly AFM storage state (Fig. 5b). This functionally represents the continuous limit of the AFM to FM transition in existing proposed AFM memory resistors like FeRh[3], where now we are able to smoothly tune between AFM and FM states instead of inducing a phase transition that only exists in certain materials.
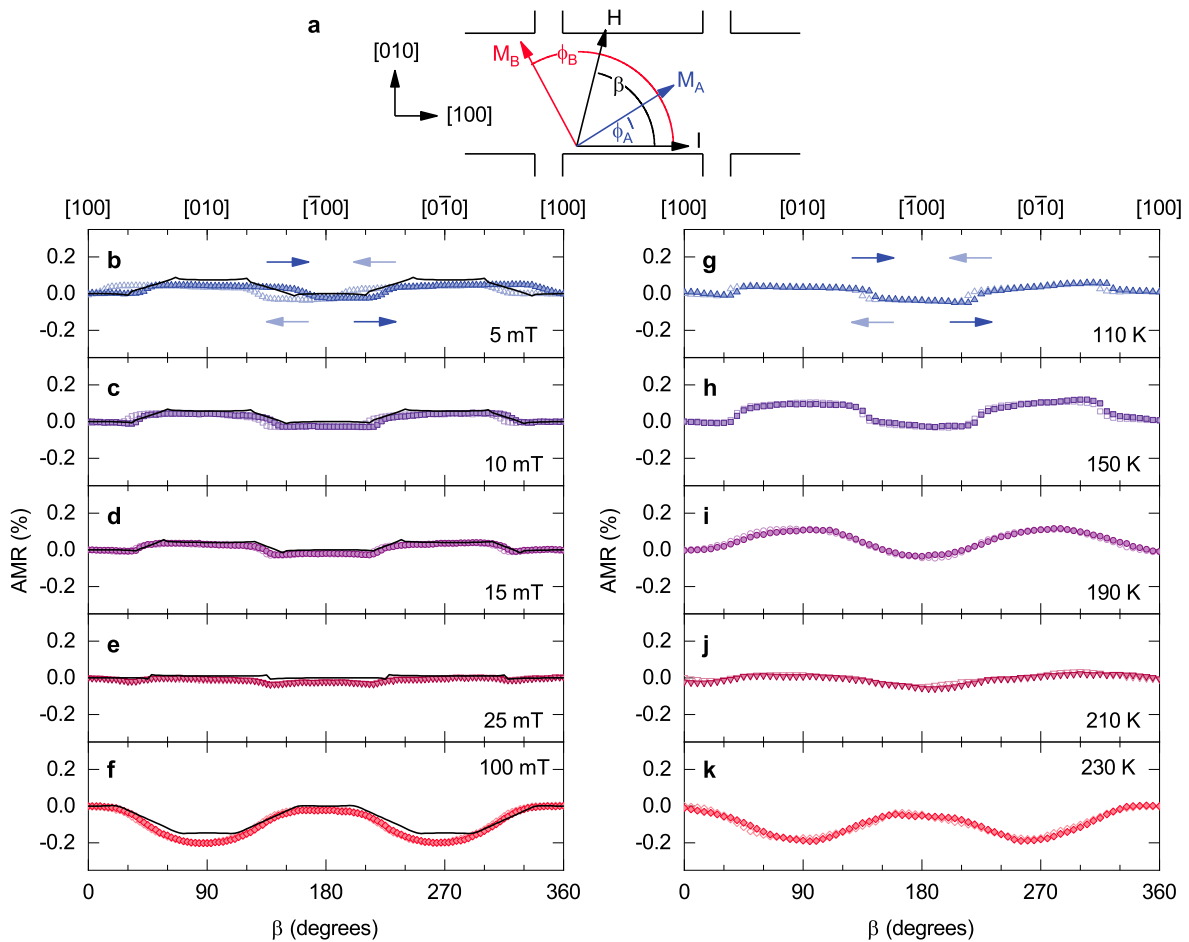
FIG. 4. **Magnetic field and temperature dependent anisotropic magnetoresistance for superlattice on SrTiO$_3$. (a)** Schematic representation of the device geometry for anisotropic magnetoresistance (AMR) measurements, with the directions of the applied magnetic field and sublattice magnetizations indicated. **(b–f)** AMR measurements on the LNO/LSMO superlattice with respect to applied field measured at 110 K. The amplitude and sign of the AMR signal shifts as the field-induced closing of the non-collinear moments goes from $\phi_M > 90°$ (b–d), to $\phi_M \sim 90°$ (e), to $\phi_M < 90°$ (f). The solid lines represents the calculated AMR response based off the parameters obtained in the free energy minimization model fitting of the PNR data. **(g–k)** Anisotropic magnetoresistance measurements on the LNO/LSMO superlattice with increasing temperature with 10 mT applied field. The phase of the AMR signal shifts 180° as the increased temperature continuously reduces non-collinearity from $\phi_M > 90°$ (g–i), to $\phi_M \sim 90°$ (j), to $\phi_M < 90°$ (k). As the temperature is increased, the magnetocrystalline anisotropy plays less of a role as can be seen as the AMR curves become more rounded. AMR $= \left[R\left(\beta\right) - R\left(\beta = 0°\right)\right]/R\left(\beta = 0°\right)$.

V. DISCUSSION

Magnetic fields are only one of several mechanisms by which the magnetic state of the superlattice can be controlled. We envision magnetic switching may also be achieved with higher efficiency using spin-transfer torque[32], or spin-orbit torque switching[4,33,34], through either direct spin injection or designed inversion asymmetry. Since these effects are difficult to achieve with purely AFM materials, the tunable non-collinear structure described here may be a route to realizing efficient AFM switching.

In conclusion, we have demonstrated that non-collinear antiferromagnetic structures in LNO/LSMO superlattices can be used as a model magnetic memory where write/read operations are carried out using only small magnetic fields and a resistive readout. Additionally, a stable "park" state, which is unique to this system, is identified where the LSMO layers are in nearly AFM alignment, thus incorporating the benefits of antiferromagnetism along with magnetic field control using relatively low fields. The continuous tunability from synthetic AFM to FM introduces a new degree of freedom to the design of AFM magnetic memories. Since our materials are artificially realized through superlattice growth, we are not limited to the intrinsic materials properties of the small number of potential AFM magnetic memory candidates. This represents a bottom up approach to AFM memory design, where we can now create new materials from existing ones, with new properties as de-
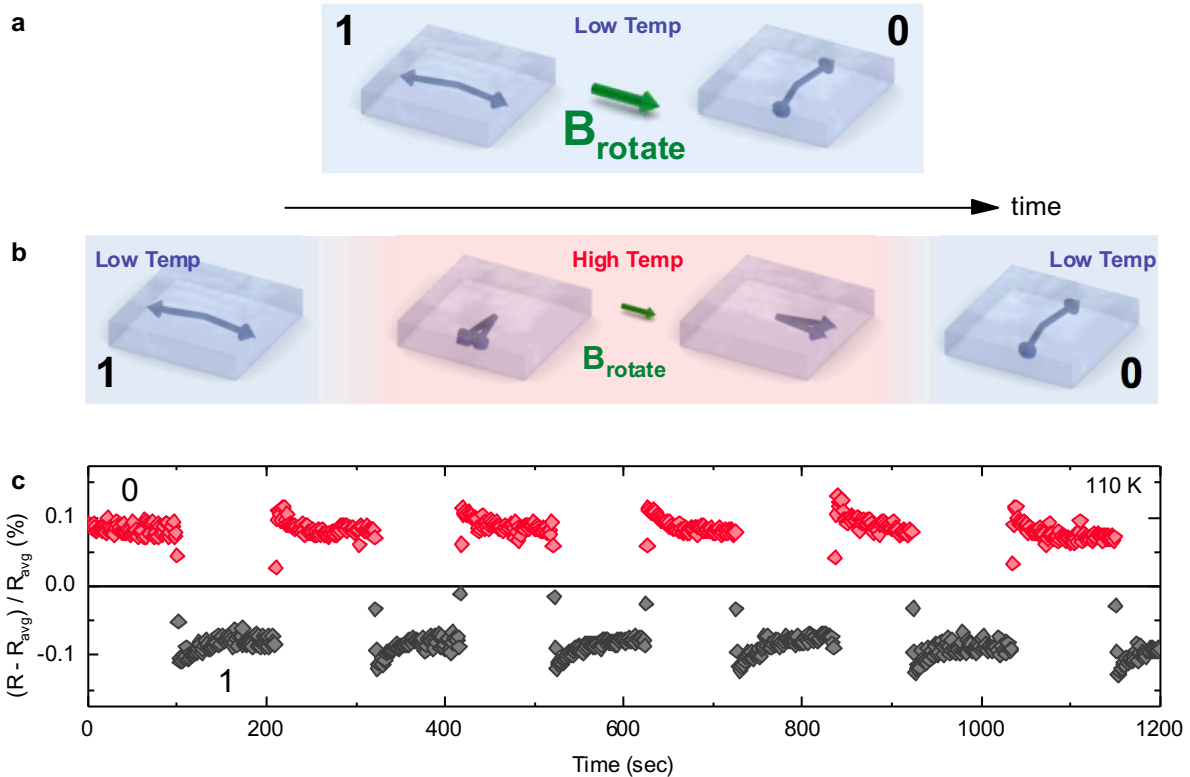
FIG. 5. **Proposed non-collinear resistive memory operation. (a)** Using induced non-collinearity to create magnetic field control of a nearly AFM magnetic structure into two states representing 0 and 1. **(b)** By heating the same memory element to reduce non-collinearity, a nearly FM magnetic structure can be continuously obtained. A smaller field can be used to rotate this FM-like structure, and subsequently cooled to the AFM-like state to retain the advantageous properties of AFM resistive memory. This operation mechanism is functionally equivalent to existing fully AFM resistive memory, but in a synthetically designed structure with continuous tuning between AFM and FM states. **(c)** Repeatable demonstration of switching between two states at 110 K, using 5 mT applied magnetic field rotated between the [100] and [010] directions, as shown in (a).

sired.

* Authors contributed equally to this work.
† anand@anl.gov
[1] T. Jungwirth, X. Marti, P. Wadley, and J. Wunderlich, "Antiferromagnetic spintronics," Nature Nanotechnology **11**, 231 (2016).
[2] X. Marti, I. Fina, and T. Jungwirth, "Prospect for antiferromagnetic spintronics," IEEE Transactions on Magnetics **51**, 1 (2015).
[3] X. Marti, I. Fina, C. Frontera, J. Liu, P. Wadley, Q. He, R. J. Paull, J. D. Clarkson, J. Kudrnovský, I. Turek, J. Kuneš, D. Yi, J.-H. Chu, C. T. Nelson, L. You, E. Arenholz, S. Salahuddin, J. Fontcuberta, T. Jungwirth, and R. Ramesh, "Room-temperature antiferromagnetic memory resistor," Nature Materials **13**, 367 (2014).
[4] P. Wadley, B. Howells, J. Zelezny, C. Andrews, V. Hills, R. P. Campion, V. Novak, K. Olejnik, F. Maccherozzi, S. S. Dhesi, S. Y. Martin, T. Wagner, J. Wunderlich, F. Freimuth, Y. Mokrousov, J. Kune, J. S. Chauhan, M. J. Grzybowski, A. W. Rushforth, K. W. Edmonds, B. L. Gallagher, and T. Jungwirth, "Electrical switching of an an-

tiferromagnet," Science **351**, 587 (2016).

[5] I. Fina, X. Marti, D. Yi, J. Liu, J. H. Chu, C. Rayan-Serrao, S. Suresha, A. B. Shick, J. Železný, T. Jungwirth, J. Fontcuberta, and R. Ramesh, "Anisotropic magnetoresistance in an antiferromagnetic semiconductor," Nature Communications **5**, 4671 (2014).

[6] S. Fukami, C. Zhang, S. DuttaGupta, A. Kurenkov, and H. Ohno, "Magnetization switching by spin-orbit torque in an antiferromagnet-ferromagnet bilayer system," Nature Materials **15**, 535 (2016).

[7] W. Zhang, M. B. Jungfleisch, W. Jiang, J. E. Pearson, A. Hoffmann, F. Freimuth, and Y. Mokrousov, "Spin Hall effects in metallic antiferromagnets," Physical Review Letters **113**, 196602 (2014).

[8] S. Seki, T. Ideue, M. Kubota, Y. Kozuka, R. Takagi, M. Nakamura, Y. Kaneko, M. Kawasaki, and Y. Tokura, "Thermal generation of spin current in an antiferromagnet," Physical Review Letters **115**, 266601 (2015).

[9] S. M. Wu, W. Zhang, A. KC, P. Borisov, J. E. Pearson, J. S. Jiang, D. Lederman, A. Hoffmann, and A. Bhattacharya, "Antiferromagnetic spin Seebeck effect," Physical Review Letters **116**, 097204 (2016).

[10] S. S. P. Parkin, N. More, and K. P. Roche, "Oscillations in exchange coupling and magnetoresistance in metallic superlattice structures: Co/Ru, Co/Cr, and Fe/Cr," Physical Review Letters **64**, 2304 (1990).

[11] M. D. Stiles, "Exchange coupling in magnetic heterostructures," Physical Review B **48**, 7238 (1993).

[12] J. Slonczewski, "Overview of interlayer exchange theory," Journal of Magnetism and Magnetic Materials **150**, 13 (1995).

[13] S. O. Demokritov, "Biquadratic interlayer coupling in layered magnetic systems," Journal of Physics D: Applied Physics **31**, 925 (1998).

[14] M. Rührig, R. Schäfer, A. Hubert, R. Mosler, J. A. Wolf, S. O. Demokritov, and P. Grünberg, "Domain observations on Fe-Cr-Fe layered structures. Evidence for a biquadratic coupling effect," Physica Status Solidi (a) **125**, 635 (1991).

[15] J. Hoffman, B. J. Kirby, J. Kwon, G. Fabbris, D. Meyers, J. W. Freeland, I. Martin, O. G. Heinonen, P. Steadman, H. Zhou, C. M. Schlepuetz, M. P. M. Dean, S. G. E. te Velthuis, J. M. Zuo, and A. Bhattacharya, "Oscillatory noncollinear magnetism induced by interfacial charge transfer in superlattices composed of metallic oxides," Physical Review X **6**, 041038 (2016).

[16] S. M. Wu, J. Hoffman, J. E. Pearson, and A. Bhattacharya, "Unambiguous separation of the inverse spin Hall and anomalous Nernst effects within a ferromagnetic metal using the spin Seebeck effect," Applied Physics Letters **105**, 092409 (2014).

[17] S. M. Wu, F. Y. Fradin, J. Hoffman, A. Hoffmann, and A. Bhattacharya, "Spin Seebeck devices using local on-chip heating," Journal of Applied Physics **117**, 17C509 (2015).

[18] B. Kirby, P. Kienzle, B. Maranville, N. Berk, J. Krycka, F. Heinrich, and C. Majkrzak, "Phase-sensitive specular neutron reflectometry for imaging the nanometer scale composition depth profile of thin-film materials," Current Opinion in Colloid & Interface Science **17**, 44 (2012).

[19] Y. Bason, J. Hoffman, C. H. Ahn, and L. Klein, "Magnetoresistance tensor of $La_{0.8}Sr_{0.2}MnO_3$," Physical Review B **79**, 92406 (2009).

[20] P. Lecoeur, P. L. Trouilloud, G. Xiao, A. Gupta, G. Q. Gong, and X. W. Li, "Magnetic domain structures of $La_{0.67}Sr_{0.33}MnO_3$ thin films with different morphologies," Journal of Applied Physics **82**, 3934 (1997).

[21] A. Rajapitamahuni, L. Zhang, M. A. Koten, V. R. Singh, J. D. Burton, E. Y. Tsymbal, J. E. Shield, and X. Hong, "Giant enhancement of magnetic anisotropy in ultrathin manganite films via nanoscale 1D periodic depth modulation," Physical Review Letters **116**, 187201 (2016).

[22] Y. Suzuki, H. Y. Hwang, S.-W. Cheong, T. Siegrist, R. B. van Dover, A. Asamitsu, and Y. Tokura, "Magnetic anisotropy of doped manganite thin films and crystals," Journal of Applied Physics **83**, 7064 (1998).

[23] K. Steenbeck and R. Hiergeist, "Magnetic anisotropy of ferromagnetic $La_{0.7}(Sr, Ca)_{0.3}MnO_3$ epitaxial films," Applied Physics Letters **75**, 1778 (1999).

[24] L. M. Berndt, V. Balbarin, and Y. Suzuki, "Magnetic anisotropy and strain states of (001) and (110) colossal magnetoresistance thin films," Applied Physics Letters **77**, 2903 (2000).

[25] A. Solignac, R. Guerrero, P. Gogol, T. Maroutian, F. Ott, L. Largeau, P. Lecoeur, and M. Pannetier-Lecoeur, "Dual antiferromagnetic coupling at $La_{0.67}Sr_{0.33}MnO_3$/$SrRuO_3$ interfaces," Physical Review Letters **109**, 027201 (2012).

[26] See Supplemental Material at [URL will be inserted by publisher] for details regarding the free energy model simulations.

[27] T. McGuire and R. Potter, "Anisotropic magnetoresistance in ferromagnetic $3d$ alloys," IEEE Transactions on Magnetics **11**, 1018 (1975).

[28] N. Naftalis, Y. Bason, J. Hoffman, X. Hong, C. H. Ahn, and L. Klein, "Anisotropic magnetoresistance and planar Hall effect in epitaxial films of $La_{0.7}Ca_{0.3}MnO_3$," Journal of Applied Physics **106**, 23916 (2009).

[29] H. X. Tang, R. K. Kawakami, D. D. Awschalom, and M. L. Roukes, "Giant planar Hall effect in epitaxial (Ga,Mn)As devices," Physical Review Letters **90**, 107201 (2003).

[30] Y. Bason, L. Klein, J.-B. Yau, X. Hong, J. Hoffman, and C. H. Ahn, "Planar Hall-effect magnetic random access memory," Journal of Applied Physics **99**, 08R701 (2006).

[31] X. Hong, J.-B. Yau, J. D. Hoffman, C. H. Ahn, Y. Bason, and L. Klein, "Effect of electric field doping on the anisotropic magnetoresistance in doped manganites," Physical Review B **74**, 174406 (2006).

[32] A. Bergman, B. Skubic, J. Hellsvik, L. Nordström, A. Delin, and O. Eriksson, "Ultrafast switching in a synthetic antiferromagnetic magnetic random-access memory device," Physical Review B **83**, 224429 (2011).

[33] L. Liu, T. Moriyama, D. Ralph, and R. Buhrman, "Spin-torque ferromagnetic resonance induced by the spin Hall effect," Physical Review Letters **106**, 36601 (2011).

[34] H. Kurebayashi, J. Sinova, D. Fang, S. C. Irvine, T. D. Skinner, J. Wunderlich, V. Novák, R. P. Campion, B. L. Gallagher, E. K. Vehstedt, L. P. Zârbo, K. Výborný, A. J. Ferguson, and T. Jungwirth, "An antidamping spin-orbit torque originating from the Berry curvature," Nature Nanotechnology **9**, 211 (2014).